Particles II

Access the latest eBook →

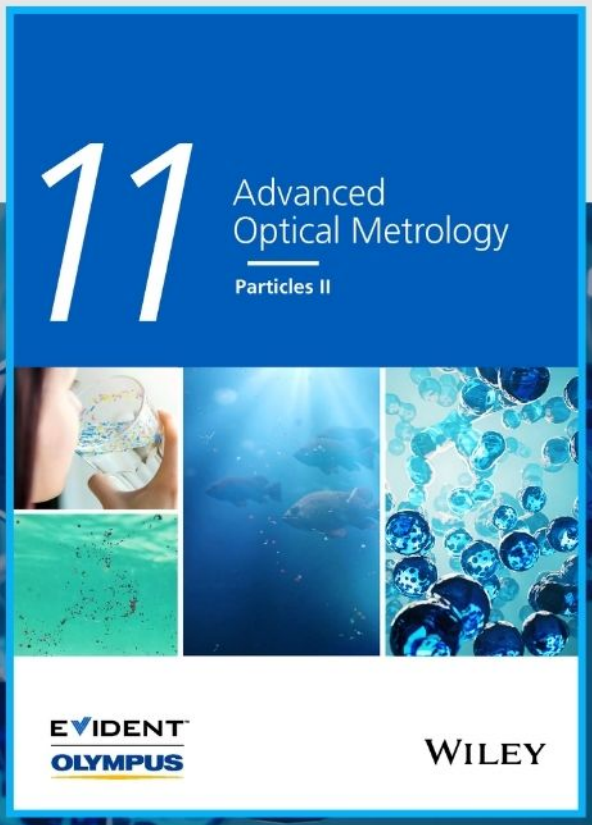

Impact on Biological Systems and the Environment

This eBook is dedicated to the research of Professor David Wertheim.
In collaboration with various groups, Professor Wertheim uses confocal microscopy to analyse the impact of different types of particles on human health and the environment, with a focus on human health-hazardous particles detected with solid-state nuclear track detectors (SSNTD). Download for free, today.

EVIDENT
OLYMPUS

WILEY

ADVANCED FUNCTIONAL MATERIALS
www.afm-journal.de

Multi-Electrode Printed Bioelectronic Patches for Long-Term Electrophysiological Monitoring

Manuel Reis Carneiro, Carmel Majidi, and Mahmoud Tavakoli**

A novel architecture of materials and fabrication techniques is proposed that serves as a universal method for implementation of thin-film biostickers for high resolution electrophysiological monitoring. Unlike the existing wearable patches, the presented solution can be worn for several days, and is not affected by daily routines such as physical exercise or taking bath. A printable biphasic liquid metal silver composite is used, both as the electrical interconnects and the electrodes. This allows combining advantages of dry electrodes, i.e., printability and non-smearing behavior, with benefits of wet electrodes, i.e., high-quality signal. A human subject study showed that these biphasic printed electrodes benefit from a lower electrode-skin impedance compared to clinical grade Ag/AgCl electrodes. Digital printing enables autonomous fabrication of biostickers that are taylor-made for each user and each application. A universal miniaturized electronic system for biopotential acquisition and wireless communication is develpoed, and demonstrated multiple biopotential acquisition cases, including electrocardiography, electroencephalography, electromyography, and electrooculography.

1. Introduction

Health monitoring systems have undergone significant developments in the last decade, mainly thanks to the advent of wearable technology, which contrasts with the bulky, rigid, and obstructive equipment commonly found in clinics and hospitals.[1] In the last few years, wearable devices were proposed for long-term and continuous electrophysiological monitoring. This includes both e-textiles or ultrathin adhesive e-skins for the recording of biopotentials (electrocardiography – ECG,[2–5] electromyography – EMG,[6–9] electroencephalography – EEG,[10–14] or electrooculography – EOG),[9,12,15] respiration rate,[16–18] temperature,[19,20] pulse oximetry,[21,22] or human motion.[23,24] The ultimate goal is to enable long-term electrophysiological monitoring, increase the patient comfort during such analysis, and to reduce the healthcare burden by enabling remote patient monitoring – an aspect to which more importance has been given after the recent COVID-19 pandemic.[25] It also allows patients to be monitored 24/7 while remaining in their homes and keeping their routines, which has been proven to speed-up recoveries while reducing healthcare costs.[26,27]

This has been a major driving force for the novel field of stretchable and thin-film electronics, which intends to develop advanced electronic systems that can adapt to the dynamic morphology of the human skin. Materials and fabrication techniques for advancement of this field have been a major focus of investigation in the past few years.[28,29] This includes techniques for implementation of deterministic structures,[30] conductive composites,[31–36] and liquid metals,[37–39] which include soft lithography,[40–44] laser patterning,[45–49] stencil printing,[12,34,44,50] or direct deposition.[16,31,32,46,49] Another requirement is the integration of skin-interfacing electrodes to collect biopotentials from the epidermis for EMG/ECG/EEG monitoring, which include the traditional Ag/AgCl electrodes, novel wet hydrogel electrodes[51,52] as well as printed dry electrodes based on carbon,[12] silver[2,12,20,53,54] or polymers such as PEDOT:PSS.[55] Incorporation of thin-film printed electrodes generally is preferable due to higher user comfort, easier implementation, a more desirable form factor, and the possibility of very low-cost and scalable fabrication. However, compared to gel electrodes, these printed dry electrodes suffer from a lower skin-conformance, a higher electrode-skin impedance, and thus a lower signal quality.[56]

In summary, implementation of a truly wearable, comfortable, thin-film, and low-cost electrophysiological monitoring system that provides a medical-grade interfacing quality is still not demonstrated. A few implementations of "electronic tattoos"[5,15,21,31,57] are valuable progress, however, these usually fall short either in terms of the required robustness for long-term monitoring, or in terms of signal quality that usually gets degraded over time due to reduced electrode-skin conformance.

M. Reis Carneiro, C. Majidi
Soft Machines Lab
Department of Mechanical Engineering
Carnegie Mellon University
Pittsburgh, PA 15213, USA
E-mail: cmajidi@andrew.cmu.edu
M. Reis Carneiro, M. Tavakoli
Institute of Systems and Robotics
Department of Electrical and Computer Engineering
University of Coimbra
Coimbra 3030–290, Portugal
E-mail: mahmoud@isr.uc.pt
The ORCID identification number(s) for the author(s) of this article can be found under https://doi.org/10.1002/adfm.202205956.

DOI: 10.1002/adfm.202205956

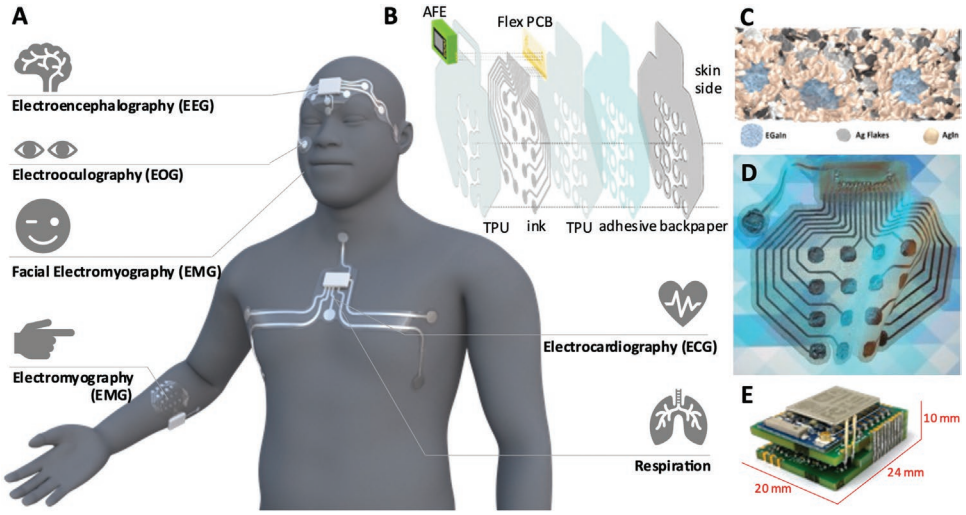

Figure 1. A) Depending on its shape and placement in the body, the proposed adhesive patches can be used for detection of multiple electrophysiological signals: brain waves (EEG), eye movement (EOG), neuromuscular activity (EMG), cardiac activity (ECG), and respiration. B) The various layers and components that compose the e-patch. C) Schematic model of the trinary microstructure of the biphasic conductive polymer. Adapted with permission from Ref. [29]. Copyright 2021 American Chemical Society. D) Fully printed flexible adhesive patch on a patterned background, evidencing the transparency of the substrate. E) Rigid analog front end.

As well, despite the progresses, there have been limited efforts to create fully-functional systems– instead, most studies focus on the synthesis and characterization of standalone electrodes.[10,13,15,51,52,55,57] Furthermore, in cases where a fully standalone patch is presented, it is typically limited to a single predefined application.[3,4,7,12,20]

In this work, we demonstrate a novel architecture of materials and methods for implementation of thin-film multielectrode adhesive patches for long-term and reliable monitoring of electrophysiological signals and digital biomarkers (**Figure 1**A,B). We show that by using a bi-phasic Ag-EGaIn composite we previously developed[32] (Figure 1C), and a multi-layer thin film (<210 µm) implementation, one can, thanks to a digital fabrication process, rapidly develop patient-specific multi-electrode biostickers that seamlessly conform to the natural roughness and contours of the human skin and can be used for a range of biopotential recording applications. Referring to Figure 1A, this includes single-lead ECG, which is also used to determine the respiration rate of the subject, multi-lead ECG, EOG, EEG, and EMG, during several days, while withstanding everyday activities such as jogging or bathing.

This is a fully standalone system, with the e-patch (Figure 1D) is connected to a small-sized analog front-end (Figure 1E) that also rests on the skin surface, allowing for true wireless biopotential monitoring of up to 16 electrodes.

A comprehensive study with ten subjects shows that these electrodes provide a signal quality better than Ag/AgCl electrodes or than the same composite without liquid metal. Although these electrodes are solid-like and non-smearing,[48] the inclusion of EGaIn droplets into the composite contributes to lower electrode-skin impedance, making this material an excellent choice for wearable epidermal electrodes as it combines the advantages of wet electrodes in terms of signal quality and skin-interfacing, and of dry electrodes (printability, low thickness and easy implementation).

2. Results

2.1. Fabrication

Figure 1B presents the layered structure of the multielectrode biopotential recording system. Referring to the figure, the system is composed of a soft patch attached to a rigid acquisition board.

The active layer of the biosticker consists of the printed conductive lines and skin interfacing electrodes made of Ag–In–Ga–SIS polymer.[32] The circuit is readily printed through direct ink writing and can be taylor-made for each user. The ink and electrodes can be printed with a resolution of <300 µm and thickness <50 µm, thus allowing for implementation of high-resolution multi-electrode bioelectronics. The active conductive layer is aligned with a thin, flexible interfacing printed circuit board and encapsulated between two layers of thermoplastic urethane (TPU; 50 µm thickness each) of the desired shape. All layers are fused together seamlessly through a heat pressing process similar to that which is used in t-shirt stamping. A pre-cut medical-grade skin-compatible acrylic adhesive (60 µm thickness) with a backing paper liner is laminated to serve as the skin-adhesion layer prior to fusion. In the TPU and adhesive layers, holes were pre-patterned in the electrode locations to allow direct electrical contact between the ink and the skin. The rigid acquisition board consists of the analog front end (AFE), processor, and wireless communication module. The interface between the electronics and the patch is established through solder joints enabling a reliable mechanical and electrical connection between both.

A conformal and robust bond with the human skin is achieved by removing the adhesive's release liner and applying light pressure to the e-skin patch. As seen in Figure 1A, depending on the shape and placement of the e-skin in the human body, various distinct signals can be recorded, such as heart activity, brain activity, eye movement, respiration, or muscle activity in different locations. Detailed material listing

and fabrication steps for both the soft e-skin patch and the rigid acquisition PCB are presented in the Experimental section.

The comfort and usability of the developed system come not only from its lightweight (the weight of the AFE board is 5.99 g, while the weight of the patch is < 8 g, depending on the application) but also from its reduced dimensions. The final patch has a maximum estimated thickness of ≈210 µm, corresponding to the laminated stack of two TPU layers, Ag–In–Ga–SIS ink, and medical-grade adhesive, while the rigid biopotential recording board measures only 20 × 24 × 10 mm, rendering it ideal for everyday use without impacting the user's movements.

2.2. Characterization

2.2.1. Skin Conformability and Comfort

To evaluate the conformability of the developed biostickers, one patch was adhered to the user's skin, and removed after one hour to be analyzed. As seen in **Figure 2**A, the sub-millimeter wrinkles and creases of the skin surface were perfectly transferred to and replicated in the medical adhesive contact surface of the patch, showing the tight conformability of the ultrathin e-skin.

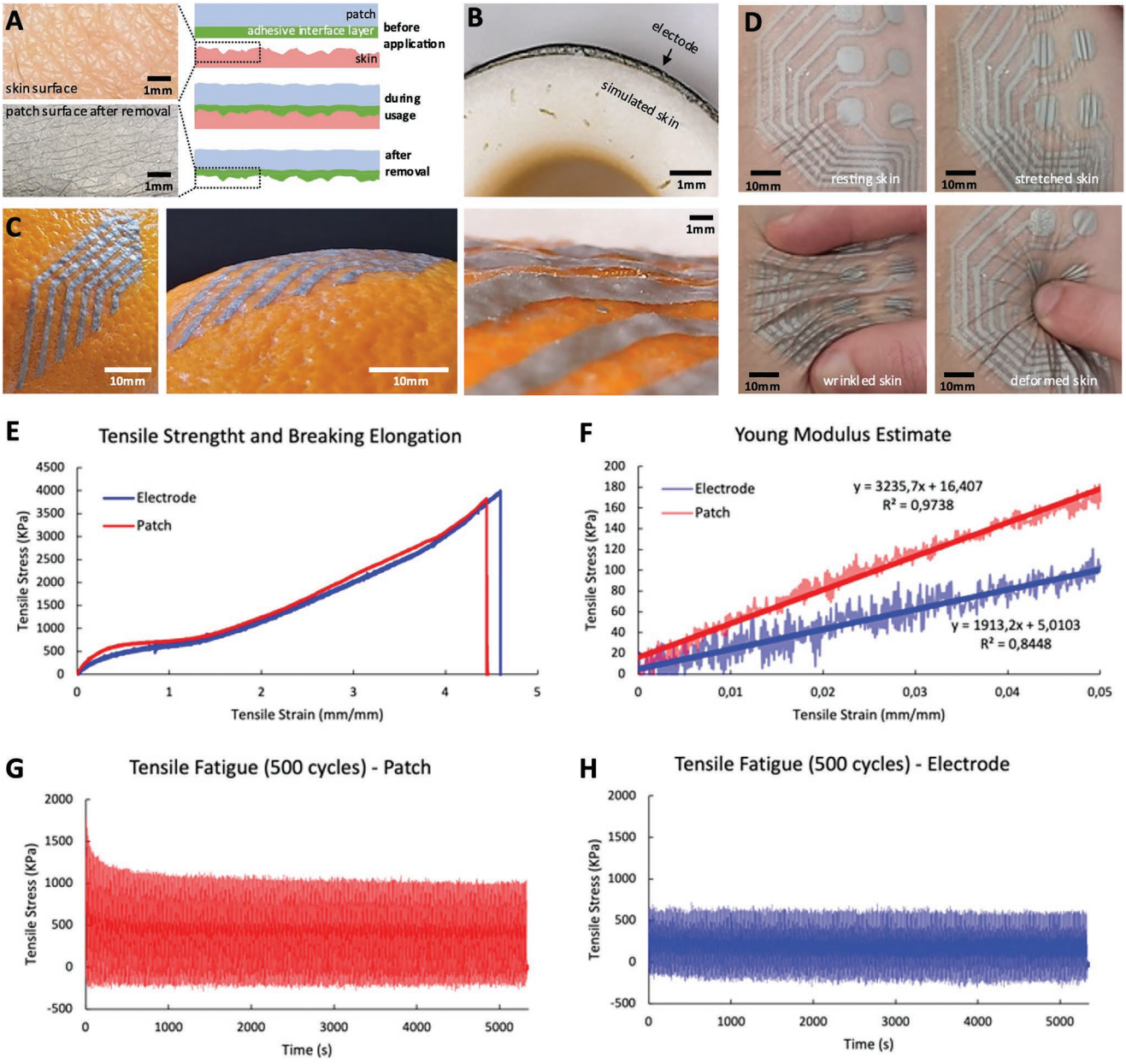

Figure 2. A) Skin wrinkles are imprinted on the adhesive interface layer of the patch. B) Cross-section image of a printed electrode conformed to a nonplanar skin replica. C) Images of a patch conformed to the rough surface of an orange peel. D) The dynamic conformal nature of the e-patch: it keeps its conformability to the skin even under deformation. E) Strain–Stress curves obtained from quasi-static tensile testing for electrode and patch stackups showing a rupture strain ≈450% for both cases. F) Young's modulus for both multi-layer stackups obtained from linear regression. G) Fatigue testing of the 4-layer patch stack for 500 cycles at a strain of 30%. H) Fatigue testing of the 2-layer electrode stack for 500 cycles at a strain of 30%. In plots E–H, one sample per test was used.

Figure 2B shows a cross-section of the skin-electrode interface. The electrode perfectly adapts to the skin surface, creating a conformal contact area for reliable biopotential measurement. Since the conductive Ag–In–Ga–SIS compound is not intrinsically adhesive, the electrode relies on the surrounding medical adhesive (which covers most of the patch contact area) to keep its conformal contact with the human epidermis.

Figure 2C further shows the conformability of the developed e-skin patch, which can conform to the complex corrugated surface of an orange peel.

We further note that the dynamic behavior of the human skin is not affected by the e-skin patch, which keeps its conformal contact with the epidermis even under extreme deformation. The patch accompanies the skin movement without signs of delamination, as seen in Figure 2D. Lastly, Removal of the patch is similar to the removal of a traditional wound dressing, and while the adhesive leaves behind some redness due to skin-pulling (as shown in Video S1, Supporting Information), this fades away after no >30 min.

2.2.2. Mechanical Characterization of the Multilayer Patch

The tensile and fatigue properties of both the full patch (4-layer stack – Figure S1, Supporting Information) and the soft skin-interfacing electrode (2-layer stack – Figure S2, Supporting Information) were evaluated using samples that follow ASTM testing standards (Figure S3, Supporting Information). Figure 2E shows that in both cases, the patch can be elongated >400% its initial size before mechanical rupture, which is much higher than strains undergone by human skin in normal conditions (≈30%[30] and ≈100% in the case of joints[58]). As well, from the strain–stress curves, we calculated the Elasticity Moduli of both stacks (Figure 2F): While the 4-layer stack shows a higher Young's modulus (E = 3.2 MPa), mainly due to the presence of the tougher adhesive layer, the 2-layer stack corresponding to the electrode presents a lower elasticity modulus (E = 1.9 MPa). In both cases, the Young's modulus of the samples is in the range of PDMS (0.1–10 MPa[59,60]), an elastomer that is traditionally used in soft electronics, as well as similar to the elastic modulus of human skin itself (≈1 MPa range[61]).

A tensile fatigue test for both layups was performed for 500 loading cycles up to 30% strain (the normal human skin stretchability). For the 4-layer patch stackup (Figure 2G; Figure S4, Supporting Information), we can observe some fatigue (decrease in the observed stress amplitude from ≈2 to ≈1.25 MPa) in the first 100 cycles (first 1100 s), that can be explained by the cracking and relaxation of the skin adhesive layer which is tougher than both the conductive ink and TPU layers. The amplitude of the tensile stress in the sample stabilizes afterward at ≈1.25 MPa.

For the case of the softer 2-layer stackup corresponding to the skin-interfacing electrodes (Figure 2H; Figure S5, Supporting Information), there is no appreciable tensile fatigue, and the measured tensile stress is stable at ≈0.9 MPa for the 500 cycles.

2.2.3. Quality of Electrode–Skin Interface

In order to evaluate the suitability of the biostickers for acquisition of clinical grade biosignals, we performed a human subject analysis to compare the quality of the skin-electrode interface when using the proposed ink electrodes, electrodes based on a similar polymer without Liquid Metal (*LM*), and clinical grade Ag/AgCl electrodes (**Figure 3**A). Each of the printed electrodes has an active contact area with the skin of 132.7 mm^2 (corresponding to a diameter of 13 mm), while the commercial Ag/AgCl electrodes presents a slightly higher contact area of 176.7 mm^2 (corresponding to a diameter of 15 mm).". The

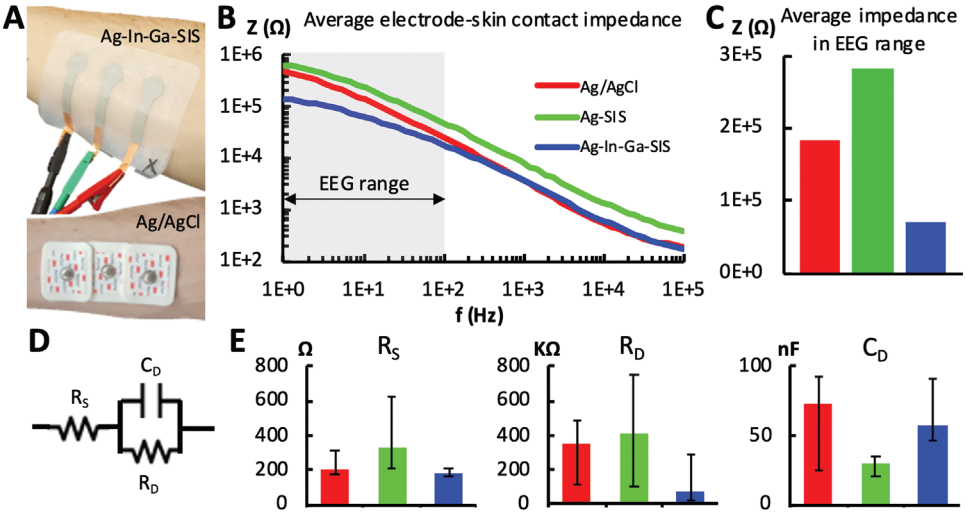

Figure 3. A) (top) Ag–In–Ga–SIS patch with each electrode having an active contact area of 132.73 mm^2 with the skin and (bottom) Ag/AgCl electrodes with each electrode having an active contact area of 176.71 mm^2 with the skin – placed on the user's ventral forearm. B) Bode plots of the electrode-skin impedance for different electrode types, averaged across the measurements for subject one to nine. C) Average impedance in the EEG range (1–100 Hz), averaged for subjects one to nine. D) Electrode–skin interface equivalent circuit. E) Equivalent circuit's parameters average for subjects one to nine and maximum/minimum error bars. (n = 1 for each of the nine subjects).

study involved ten healthy adult subjects with no prior history of skin conditions (eczema, psoriasis, etc.) and no signs of erythema in the forearm region at the time of the study. The study consisted in capturing the Bode plots for the electrode–skin interface impedances (Figure S6, Supporting Information) measured in the right inner forearm for each subject in the 1–1 × 10^5 Hz range for each electrode type. The ventral forearm was chosen for its accessibility and for being a region with low capillary density, following similar studies in the literature.[12,56] By observing the impedance data for the different subjects, we notice that for most subjects (Figures S1–S9, Supporting Information), the measured impedances for all electrodes are between 10^2 and 10^6 Ω, and the bode plots show a smooth curve, while for subject ten, the measured impedances are between 10^3 and 10^8 Ω and the curves (mainly the ones regarding Ag–SIS and Ag–In–Ga–SIS electrodes) show spikes associated with noisy measurements.

In the EEG range (1–100 Hz), shown in Figure S7 (Supporting Information), the Ag–In–Ga–SIS electrodes show a lower impedance than the Ag/AgCl counterpart for subjects one to nine. In contrast, for subject ten, this trend is inverted, with Ag/AgCl showing the lowest impedance of the three compared materials. This outlier behavior observed in subject ten is linked with the fact that this subject presented a higher-than-average hair density in the tested site: the adhesive and gel-like properties of the Ag/AgCl electrodes allowed this material to flow between the hairs and maintain a decent contact with the subject's skin. In contrast, the Ag–SIS and Ag–In–Ga–SIS electrodes (non-adhesive per se) could not interface well with the underlying skin due to the high-density hair barrier leading to noisier and higher impedance measurements. Further analysis will focus solely on subjects one to nine, excluding the outlier, subject ten, concluding that the proposed electrodes are unsuitable for skin areas with extreme hair density. Figure 3B shows the average electrode skin impedance plot for subjects one to nine, where we can observe that Ag–In–Ga–SIS electrodes show a lower impedance at lower frequencies, a trend observed in most of the tested subjects. The only case where this trend is not evident is with subject nine, in which the Ag/AgCl electrodes show a slightly lower impedance than the ink counterparts. In Figure 3C the average electrode skin impedance in the EEG range (1–100 Hz), averaged for the first nine subjects, is shown, and the previous trend is confirmed: while Ag/AgCl show an average impedance of $1.84 \times 10^5 \pm 1.09 \times 10^5$ Ω, the Ag–In–Ga–SIS electrodes show an impedance of only $6.99 \times 10^4 \pm 7.52 \times 10^4$ Ω in the same range. The Ag–SIS polymer shows the highest impedance overall ($2.81 \times 10^5 \pm 3.15 \times 10^5$ Ω in the EEG range).

These results clearly show the advantage of inclusion of *LM* in the conductive composite. While this biphasic ink is printable and non-smearing, similar to other dry electrodes made with particle-filled composites, it has a considerably lower electrode-skin impedance, when compared to the same composite without *LM*. Surprisingly, these electrodes showed also lower impedance than medical grade Ag/AgCl electrodes. This can be associated with several factors including the compliance of the electrode itself, and the thin-film structure of the biostickers, which adapts well to the wrinkles of the skin.

Figure 3D depicts the equivalent electrical circuit for the electrode–skin interface proposed in,[62] where Rs is linked to the resistance of the electrode material and the electrical path between electrodes through the living tissues, Rd corresponds to the interface resistance between the electrode and the skin, and Cd is the interface capacitance due to moving charges in the electrode–skin interfaceelectrode–skin interface. The equivalent impedance for the presented circuit is given by Equation 1

$$Ze = Rs + \frac{Rd}{1 + j2\pi f Cd\, Rd} \tag{1}$$

From the literature,[56] low Rd and Rs values and high Cd values are desirable to achieve the lowest possible impedance.

Using Equation 1, the circuit components (Rs, Cd, Rd) can be estimated from the Bode plot curves, as shown in Figure S8 (Supporting Information) for each tested subject. Figure 3E shows the average value of each component in each electrode type for the tested subjects (excluding the outlier subject 10). Regarding Rs, Ag–In–Ga–SIS electrodes show the lowest resistance (183.8 ± 21.9 Ω), followed by Ag/AgCl (199.1 ± 112.5 Ω) and finally Ag–SIS (334.6 ± 286.9 Ω).

In terms of Rd, the trend is similar to Rs, with Ag–In–Ga–SIS electrodes showing the lowest value (78.8 ± 212.6 KΩ), followed by Ag/AgCl (350.3 ± 237.9 KΩ).and Ag–SIS (407.6 ± 305.9 KΩ). In terms of Cd, Ag/AgCl electrodes present the best values (72.5 ± 48.1 nF), followed by Ag–In–Ga–SIS (57.2 ± 34.1 nF) and, lastly, Ag–SIS (29.1 ± 8.2 nF).

The low resistances In the Ag–In–Ga–SIS electrodes can be explained by the high electrical conductivity of the composite itself (7.02 × 105 S m^{-132}) as well as the conformable interfacial contact of the patches with the skin. Compared to Ag-SIS, the biphasic composite (with Ga–In alloy) shows a much lower interface resistance which we attribute to the increase in conformability due to the presence of the Ga-base alloy, a liquid metal with high wettability.[63,64]

In terms of the contact capacitance, the gel present in Ag/AgCl electrodes acts as a suitable dielectric in the electrode-skin bilayer and its intrinsic adhesiveness increases the contact area with the skin, resulting in the highest Cd value. The Ag–In–Ga–SIS, while not having a dielectric layer, still exhibits a capacitance that, although lower, is within the same order of magnitude as that of the Ag/AgCl. The comparable capacitance is attributed to the conformability and compliance of the material, which allows for increased contact area (proportional to the capacitance value as explained in[56]). The lower capacitance of Ag–SIS is attributed to the absence of Ga–In since the liquid metal may improve the surface contact area between electrodes and the skin by filling microscopic interfacial gaps that can arise from the skin creases and roughness.

To understand the aging of Ag–In–Ga–SIS polymer, an adhesive patch with five printed tracks (80 mm length and 5 mm width) was fabricated and worn by a subject for 3 days. During these days, the subject did normal daily activities including sleeping, running (45 min run under direct sunlight with an ambient temperature of 25 °C, leading to sweating), and daily showering. At the end of day 3, the average line's resistance was 2.8 (± 0.5) Ω, compared to 0.62 (± 0.42) Ω at the beginning of the test, as can be observed in **Figure 4**A. This value is still an acceptable value for digital circuits. As shown in the calculations presented in Supporting Information (Equations S1 and S2,

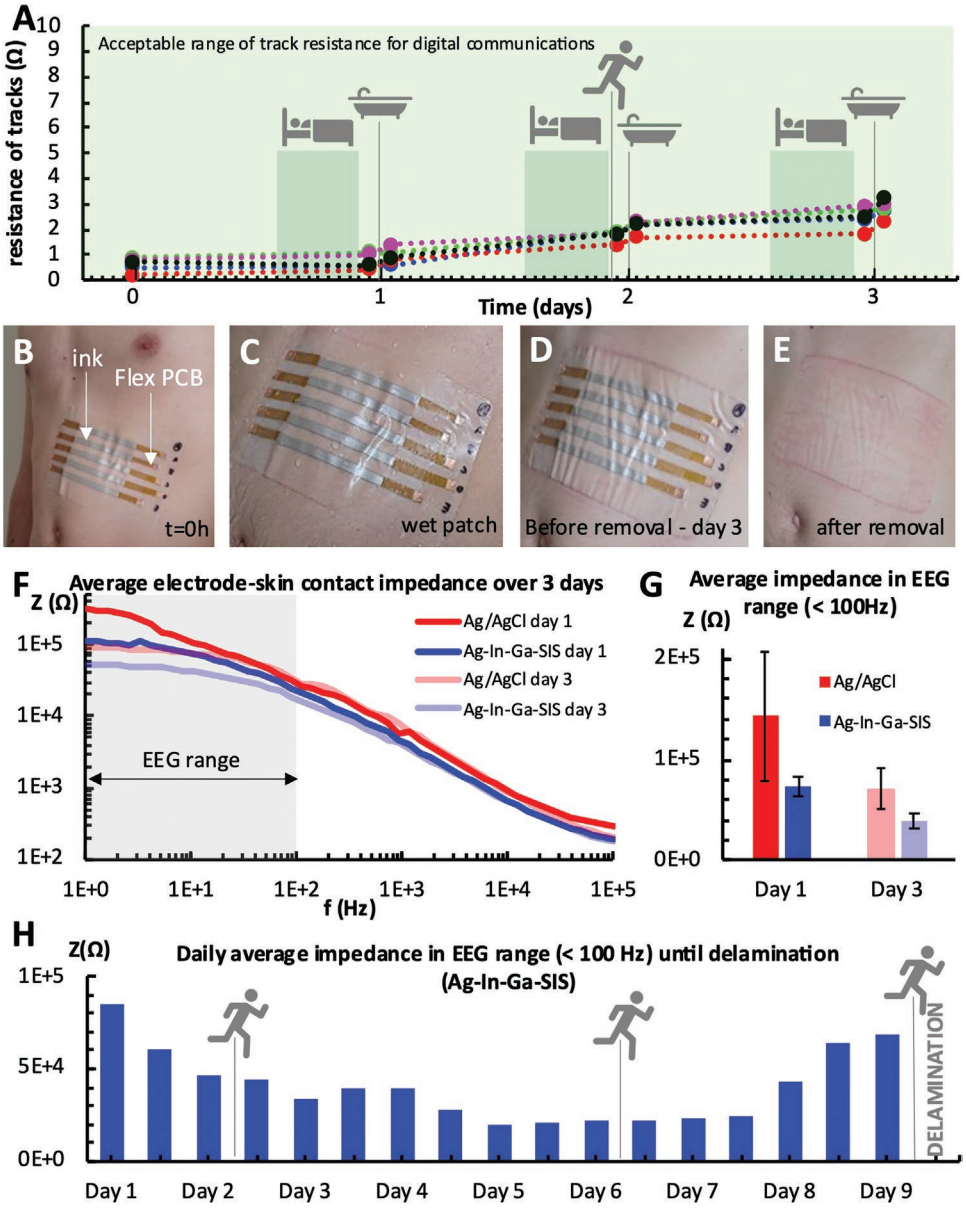

Figure 4. Aging of patch. A) Variation of ink resistance over 3 days for five samples, while performing everyday activities such as sleeping, jogging, and showering. B) Patch with printed Ag–In–Ga–SIS conductive lines with flexible contacts for easy measurement of resistance, adhered to the subject's abdomen ($t = 0$ h). C) Wet patch after showering ($t = 24$ h). D) Patch right before removal ($t = 73$ h). E) skin redness after patch removal. F) Evolution of electrode-skin impedance over the course of 3 days for standard Ag/AgCl electrodes (176.7 mm^2 contact area per electrode) and printed Ag-In-Ga-SIS electrodes (132.7 mm^2 contact area per electrode) – averaged for three measurements with distinct electrode sets. G) Average electrode-skin impedance for Ag/AgCl electrodes and printed Ag–In–Ga–SIS electrodes in the EEG range over the course of 3 days – averaged for three measurements. H) Average impedance of Ag–In–Ga–SIS electrodes (132.7 mm^2 contact area per electrode) measured twice a day until delamination of the patch on day 9. Single measurements were taken for one user and the test included daily showering, three 45 min runs and normal daily activities.

Supporting Information), our circuits are functional even for a resistance of tracks of ≈10 Ω, For practical applications, such a slight increase in track resistance (which are much lower than the resistance observed in the electrode–skin interface) would not affect the functionality or signal quality in the system.

Figure 4B shows the fabricated patch laminated in the user's abdomen.

The highest slope in the resistance curves is observed after bathing. This can be explained due to the TPU substrate of the patch swelling with humidity and bringing moisture in contact with the encapsulated ink. The wet patch is shown in Figure 4C.

Lastly, no delamination was observed during the 3 days (Figure 4D). When removing the patch, slight skin redness due to skin pulling is observable (Figure 4E), which faded away in <30 min. Otherwise, no skin irritation or inflammation from an adverse reaction to the biostickers materials was observed.

To evaluate the long-term electrical stability of the electrode skin interface, a user wore two distinct types of electrode sets

(Ag-In-Ga-SIS and Ag/AgCl) for 3 days. Since skin impedance varies over time and in different body locations, both electrode sets were placed at the same time as close as possible to each other in the user's forearm as depicted in Figure S9 (Supporting Information). The electrode-skin impedance was then measured for each electrode set after being initially placed and after being worn for 72 h. No protective layer between the electrodes and the external environment was used so that we could easily access the electrode's conductive contacts for measurements and assess how external factors impact the electrode performance (mechanical deformation and fatigue, humidity, sweating, etc.).

A similar routine as before, including sleeping, running, and showering, was performed, and the test was repeated thrice on distinct days, with electrodes fabricated from separate batches of conductive composite. In Figure 4F, the bode plot corresponding to the average electrode-skin impedance on the three trials is shown. The results for each trial are shown in Figure S10 (Supporting Information). As shown in the large-scale trial with volunteers, right after application, the Ag–In–Ga–SIS electrodes show on average a lower interface impedance than the Ag/AgCl counterpart, which is more noticeable at lower frequencies. While the average impedance for the EEG range (Figure 4G) of the Ag/AgCl electrodes on day 1 is 1.43×10^5 Ω, it is only 7.24×10^4 Ω for the polymeric electrodes. Contrary to what would be expected, none of the electrodes showed signs of degradation after 3 days, and the impedance of the electrode–skin interface decreases further. This observation was attributed to the buildup of sweat and moisture that gets trapped on the interface. This accumulation of electrolytes between the electrode and the skin further facilitates the movement of charges, thus decreasing impedance in the first couple of days. It is also relevant to note that the Ag/AgCl electrodes show a higher standard deviation of the impedance on the EEG range than the printed electrodes, which can be associated with the repeatability and stability of the Ag–In–Ga–SIS polymer and printing methodology across batches. Once again, no skin irritation or inflammation was observed in the sites where the Ag–In–Ga–SIS electrodes contacted the skin after 3 days of being worn.

Another experiment was performed to determine durability of the patch over the skin without de-lamination or electrical failure. For this test, a printed three electrode patch (Figure 3A top) was placed on the user's forearm and worn daily until it would fail. Impedance measurements were taken twice a day right after the subject woke up in the morning, and after showering in the afternoon (10 h apart), and the patch was exposed to warm running water during showering and to mechanical friction from clothes and during sleeping and other daily activities. Additionally, on days 2, 6, and 9, the user went for a run outside, under direct sunlight, with ambient temperatures in the 27–30 °C, which lead to sweating and physical deformation of the patch during motion. From Figure 4H, which shows the average impedance in the EEG range (<100 Hz) for each measurement, we can observe that the electrode-skin impedance decreases on the first 4 days of use (from 8.51×10^4 to 2.76×10^4 Ω), stabilizing in the $1.91–2.47 \times 10^4$ Ω range between days 5 and 7, which can be explained, as before, by the buildup of sweat and moisture and consequent increase in electrolytes at the electrode–skin interface. Afterward, on days 8 and 9, the impedance starts increasing toward the initial values (6.91×10^4 Ω on day 9), which can be explained by the buildup of dead skin cells on the skin surface due to poor hygiene at the interface. Finally, it was observed that the patch started delaminating on day 9 during showering and although it did not completely delaminate by itself, the test was stopped, since full conformal contact with the skin was lost. Slight redness was observed which disappeared after ≈1 h.

As described above, the patch was subject to harsh conditions, including direct contact with running water and moisture during daily showering, sweat buildup on the skin surface due to physical activity, and rubbing against clothing. Nevertheless, no delamination of the electrodes or displacement/detachment of the rigid boards was observed until 9 consecutive days of use. Moreover, as we have shown, the buildup of sweat in the electrode–skin interface even led to a decrease in electrode-skin impedance on the first 4/5 days of use, stabilizing at low values until the 8th day. On the 8th day of use, we start observing a new increase in impedance due to deterioration of the interface and the patch failed due to delamination on day 9.

2.3. Applications

The presented architecture of materials and fabrication techniques allow to rapidly fabricate biostickers for various applications, such as EMG, EEG, EOG, or ECG. The possibility of digital printing permits to adjust the number and the geometry of the electrodes based on the applications and the user size. The external electronics remain the same for the various applications, while the biosticker can easily be changed and discarded.

Here, we show the acquisition of multiple digital biomarkers: single lead ECG, multi-lead ECG, Facial EMG, EOG, EEG and finally limb EMG.

2.3.1. Single-Lead Electrocardiography

A one-lead ECG acquisition patch prototype was fabricated as the simplest use case scenario. As depicted in **Figure 5**A, it is composed of two recording electrodes (Figure 5B), one reference electrode, and a right leg drive electrode (RLD). Figure 5C depicts a portion of the acquired ECG signal from a healthy subject, where the standard features of such a signal can be observed: the QRS complex, as well as *P* and *T* waves, are labeled in the figure. The *RR* interval (corresponding to the time between two consecutive R peaks) was calculated as being 790 ms, from which a heart rate of 76 bpm can be estimated. Furthermore, we can observe that the duration of the QRS complex is <0.1 s and the time interval between *Q* and *T* waves falls below the limit of 0.4 s. From these characteristics, we were able to validate and infer the good quality of the recorded signal since all referred features and duration of waves fall within the limits stipulated by physicians for considering a normal ECG.[65] The real-time acquisition of the one-lead ECG is shown in Video S2 (Supporting Information).

For this application, the subject wore the ECG patch for 3 days while keeping their usual daily routine. The signals recorded from day 1, after the patch was first adhered to the

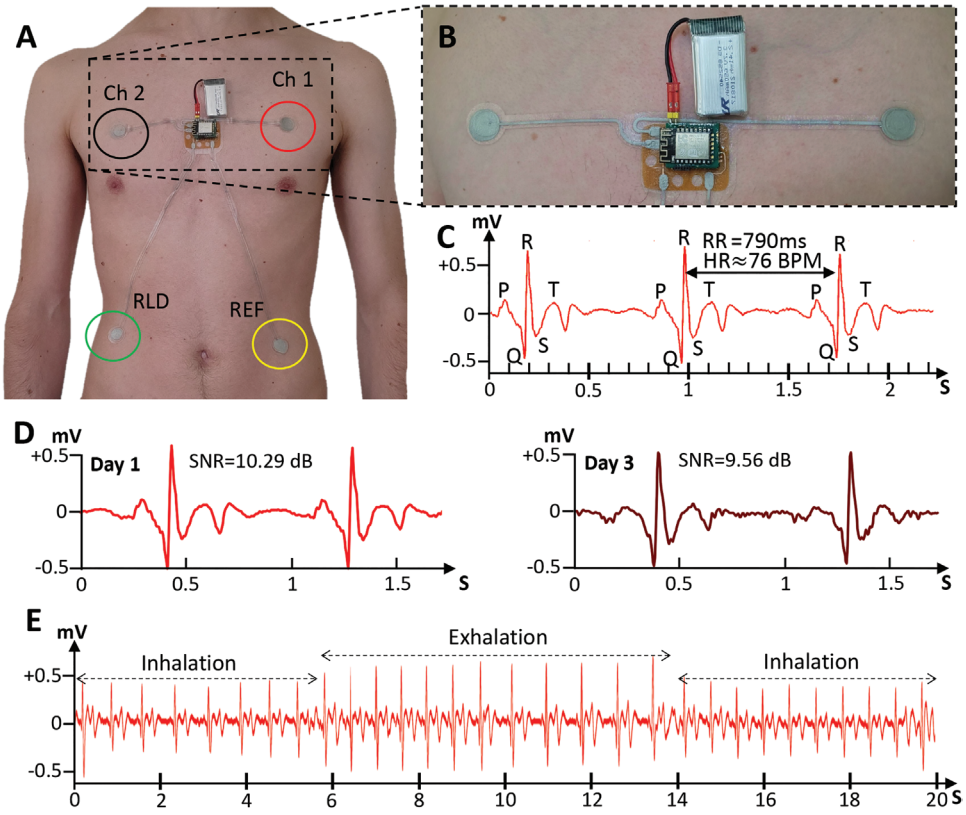

Figure 5. A) Electrode positioning for one-Lead Electrocardiography patch. B) Close-up image of the patch showing the two measuring electrodes, analog-front-end, and battery. C) Acquired ECG signal and identification of normal ECG features such as the QRS Complex and *P* and *T* waves. An *RR* interval of 790 ms, from which a heartrate measurement of 76 bpm can be derived. D) Comparison between ECG signal on 1st day and after 3 days of the patch being used. Although Signal to Noise Ratio decreases, normal ECG features are still visible. E) Respiration signal can be derived from the ECG measurement thanks to the change in amplitude of the QRS complex during respiration cycles.

skin, and after 72 h are shown in Figure 5D. Although the Signal to Noise Ratio (*SNR*) decreases slightly throughout the test duration (from 10.29 to 9.56 dB), all the typical ECG features are still visible on the signal recorded from day 3 and the *RR* interval, and heart rate can still be accurately calculated, despite the appearance of noise artifacts.

Although the electrode–skin interface impedance is observed to decrease 0.73 dB between days 1 and 3, such a slight decrease does not impact the signal quality for observation and analysis of the ECG features. Since the electrode-skin impedance is shown to decrease during the first few days of wearing the system, the slight decrease in *SNR* in the signal recorded in Day 3 is not expected to arise from the electrical interface with the electrodes. Instead, such a decrease in *SNR* could be explained by the presence of high-frequency muscle movement artifacts that may have happened during recording on Day 3 leading to the slightly increased noise amplitude at that moment. Longer-term ECG measurements in more patients should be performed in future studies to assess the concrete origins of noise and artifacts in the system.

It was also observed that the user's respiratory activity could be derived from the ECG recordings, as depicted in Figure 5E. An increase in the amplitude of the QRS complex is related to exhalation. In contrast, when the user inhales, the amplitude of the QRS complex decreases. We hypothesize that this observation is due to the changes in impedance of the thoracic cavity during the respiration cycle, as well as to the stretching of the printed conductive lines acting a strain gauge, which leads to amplitude modulation of the ECG signal. We can observe in the plot from Figure S11 (Supporting Information) that the resistance of Ag–In–Ga–SIS printed lines in the patch is dependent on the applied strain, acting as a strain gauge. This resistance change, although small (≈1 Ω for a strain of 30%), is associated with the volume changes of the thorax and is enough to modulate the amplitude of the ECG signal, thereby allowing for visualization of the respiration cycles.

2.3.2. Multi-Lead Electrocardiography

As a slightly more complex use case, a multi-lead ECG patch was fabricated based on the EASI electrode configuration[66] (**Figure 6**A–C). This system has the advantage of being able to derive all 12-lead measurements seen in a standard ten electrode ECG (Figure 6D) by using only six electrodes and storing just three distinct signals instead of 12. These characteristics make the EASI montage ideal for telemetry and wearable systems in which storage capacity or transmission bandwidth is limited. This also permits reducing the number of electrodes for easier deployment and long-term comfort of the user.

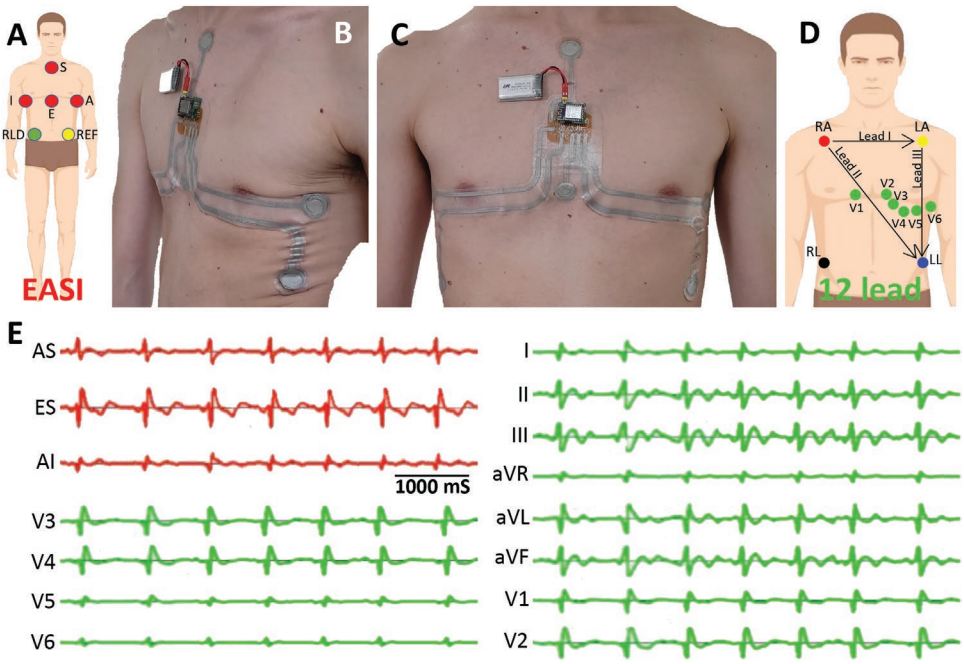

Figure 6. A) Position of ECG recording electrodes according to the EASI montage. B,C) Multielectrode ECG patch based on the EASI system. D) Position of the ECG recording electrodes in a conventional 12-lead system. E) Electrocardiogram signals directly acquired from the EASI patch (in red) and full 12-lead ECG derived from the EASI recordings (in green).

Figure 6E and Video S3 (Supporting Information) depict in red the three leads acquired from the EASI montage (AS, ES, AI) and the derived 12-lead ECG in green. Features such as the QRS complex (normal sinus rhythm) can be observed in all signals, and as well the *RR* interval shows to be regular in all traces. These are characteristics of a normal adult 12-lead electrocardiogram, as stated in.[67] Apart from the regular *RR* interval (indicating the absence of arrhythmia[67]), the heart rate can also be calculated to be ≈77 bpm, between the 60 and 100 lower and upper boundaries considered normal.[67] The equation and coefficients to perform the transformation between the EASI and the 12-lead ECGs are presented in the Experimental section.

2.3.3. Electroencephalography, Electrooculography, and Facial EMG

A patch containing ten electrodes was fabricated for recording brain activity, eye movement, and facial muscle activity. **Figure 7**A depicts the placement and function of each electrode. Figure 7B shows a user wearing the patch on their forehead and face. The simple and inexpensive digital fabrication process enables the fabrication of patient-specific patches with precise electrode positions and a custom layout that fits each user perfectly.

Figure 7C shows an example of a recorded EEG signal in which the Berger effect[68] can be observed. This effect consists of suppression of the Alpha rhythm (≈8–13 Hz) when the user opens their eyes, leading to a lower amplitude signal when compared to the brain activity while keeping their eyes closed. Figure S12A,B (Supporting Information) shows the frequency spectrums for the open and closed eyes signals, respectively, and a frequency peak can be observed ≈10 Hz when the user closes his eyes but is suppressed when the eyes are open.

This observable difference in the two signals enables a clear separation between the two states. Although it is usually more noticeable in electrodes placed on the back of the scalp, we were still able to observe this with a signal acquired from the user's forehead.

Figure 7D and Video S4 (Supporting Information) depict EOG signals that were acquired. We can observe that the left and right electrodes show opposite polarities when lateral eye movement is detected. On the other hand, eye blinks, predominantly vertical movements, are detected with higher amplitude by the EOG electrode placed below the user's eye. These are characterized by their high amplitude and low frequency.

Finally, sEMG artifacts derived from masticatory movement (Figure 7E) are detected in the face by the electrode placed near the masseter muscle. These are characterized by both high amplitude and high frequency.

Overall, possible applications of this patch include fast deployable EEG exams for emergency or ambulatory settings, sleep monitoring, and staging or human/brain–machine interfaces. Moreover, the possibility of recording muscle activity in the face (and specifically near the jaw), has relevance for monitoring orthodontia-related conditions such as bruxism or temporomandibular joint disorder, as discussed in Ref. [69]

2.3.4. Electromyography and Hand Pose Signature

Figure 8A shows an EMG patch with 17 electrodes. The patch is composed of 16 recording electrodes connected to eight

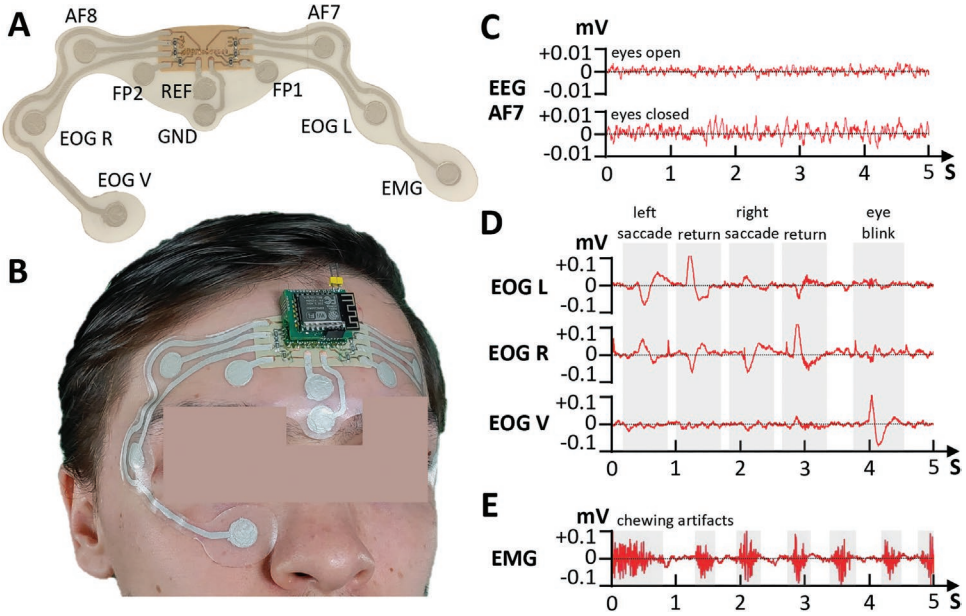

Figure 7. A) EEG/EOG/EMG patch and identification of the electrodes. B) Placement of the patch in the user's face and forehead. C) Berger effect in EEG waves. When a user opens their eyes, the alpha rhythm is attenuated in amplitude. The higher amplitude of the acquired EEG signal when the user keeps their eyes closed can be observed in the plots. D) Eye movement detection through the EOG electrodes placed near the eyes. We can observe that the left and right electrodes show opposite polarities when lateral eye movement is detected. Eyeblinks, which are a predominantly vertical movement, are detected with higher amplitude by the EOG electrode placed below the user's eye. E) Muscle artifacts from masticatory movement detected recorded by the EMG electrode placed on top of the masseter muscle.

differential acquisition channels and placed on the proximal portion of the anterior right forearm of the user and a ground electrode that lays in the user's elbow. As a sanity check, a handgrip dynamometer (Figure 8B) was used to measure the relation between EMG intensity and gripping strength. The results, shown in Figure 8C, show that, as expected, the amplitude of the acquired and rectified EMG signal (in one of the channels) increases as the grip strength increases.

Taking advantage of the high channel count, we evaluated the feasibility of using the developed patch to detect hand gestures. In Figure 8D, we can observe that for different hand poses (*P1* to *P6*), the acquired EMG signals in each channel show distinct amplitudes (only three of the eight channels are shown). For simplicity, we chose to only use the average signal amplitude in each channel as the features to differentiate between hand-poses (in one-second windows without overlapping). This simple feature vector has the advantage of being easy to extract and compute while generating small-sized datasets, thus being ideal for slow microcontroller-based systems where either power, processing, or memory are limited.

As shown in Figure 8E, for each of the eight channels, the extracted average signal amplitude was scaled to a percentage where 100% corresponds to the maximum average amplitude detected in that channel.

Figure 8F, shows 12 distinct hand gestures and the respective amplitude footprint from the EMG signals in the eight channels. Overall, clear differences can be observed between most gesture pairs. The most similar cases can be observed to be the distinction between poses four and ten and seven and eight, corresponding to cases where the gestures are similar, i.e., only showing differences in the position of one finger.

Figure S13A (Supporting Information) shows the dissimilarity coefficient between gesture pairs (computed using the Spearman correlation-based dissimilarity coefficient, i.e., the spearman distance between feature vectors of each pose observation, averaged across three one-second windows). While high dissimilarity values between pairs of gestures indicate an easy distinction between those poses (as is the case of the pair six and 12), dissimilarity coefficients as low as 0.1[70] or 0.2[71] have previously shown good results in automatic EMG hand gesture classifiers. Overall, 85% of the gesture pairs show a dissimilarity coefficient >0.2, while the average dissimilarity is 0.342. The average correlation coefficient for the same gesture across three repetitions (Figure S13B, Supporting Information) is >0.75 for all 12 poses, meaning that the system shows good repeatability.

A similar work using an equivalent EMG electrode montage[71] has been able to distinguish only between six hand gestures with a classification accuracy of ≈95% on 12 participants. The present work improves these results not only in terms of correlation coefficients but also due to the use of a considerably simpler (in terms of features extracted from the EMG signal) and more wearable system. We conjecture that the increased conformability and skin compliance of our system, as well as the low electrode-skin impedance, leads to a better acquired EMG signal and thus a more robust distinction between a larger set of gestures. As such, a good gesture classification accuracy using machine learning algorithms would be expected for our 12-poses dictionary.

Apart from being conventionally used to assess functionality and integrity of muscular activity, surface EMG has also been

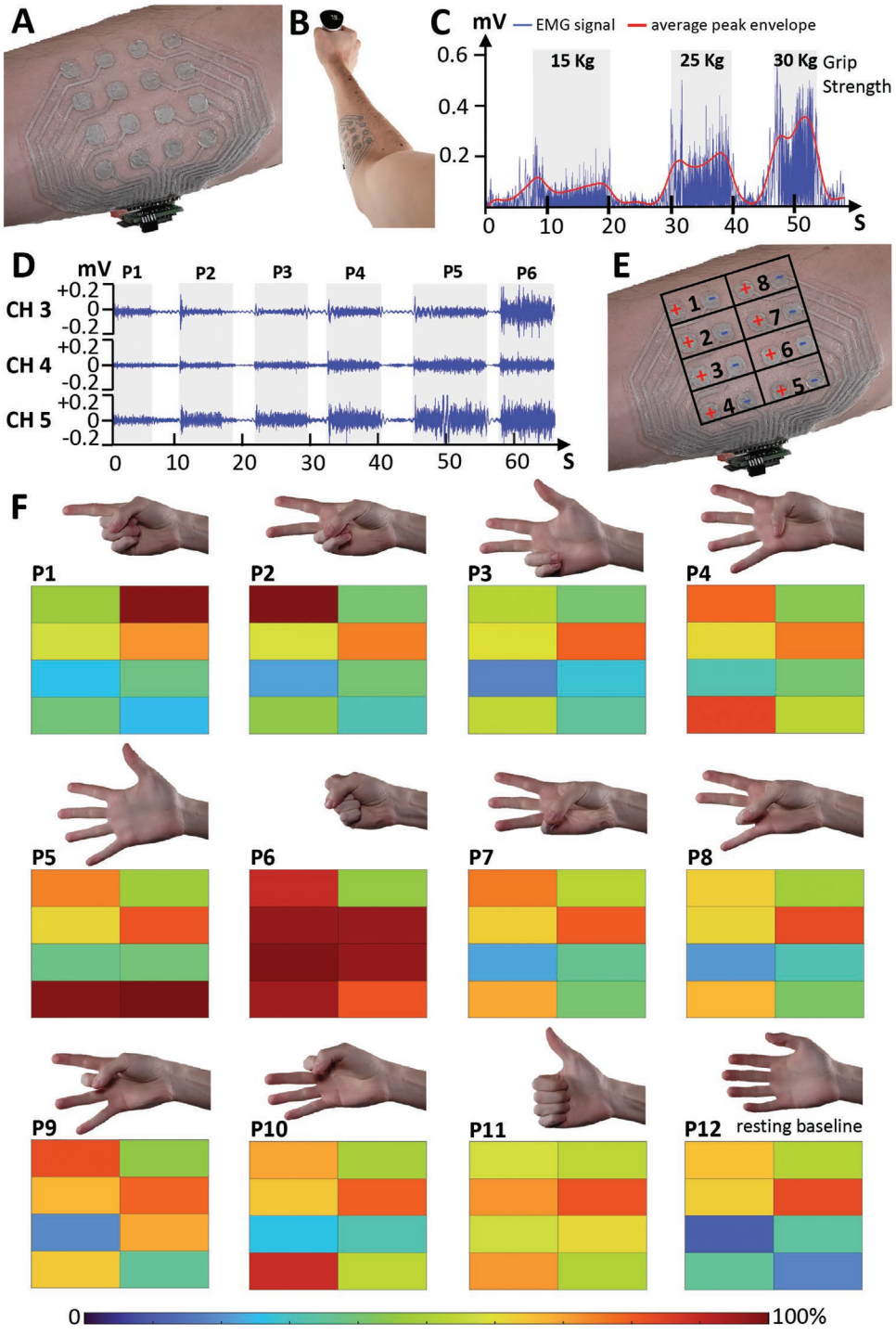

Figure 8. A) 16 electrode EMG patch. B) Setup for gripping force measurement with the EMG patch placed on the proximal portion of the anterior right forearm of the user, while grabbing a hand grip dynamometer. C) EMG signal (channel four) after full-wave rectification for different gripping forces and averaged peak envelope. D) EMG signals acquired from three channels for six distinct hand poses. E) Channel positions and polarity of the electrodes on the EMG patch placed on the right forearm. F) Scaled average amplitude of the eight EMG signals for 12 distinct hand poses.

increasingly used to directly control limb prosthetics. The fact that we are capable of detecting and classifying 12 distinct hand gestures, as well as estimating force output from EMG signals acquired by an ultrathin skin-conformal adhesive patch, paves an important step toward decreasing the cost and widening the availability of muscle-machine interfaces that provide the user with higher comfort and a larger combination of poses for a more natural control of a limb prosthetic.

3. Discussion

In this study, we presented a disposable ultrathin multi-layer adhesive patch with digitally printed skin-interfacing electrodes and interconnects based on an Ag–In–Ga filled elastomer, which conforms tightly to the natural wrinkles and creases of the human skin even during normal deformation. Tensile testing showed that the patch exhibits an elastic modulus similar to the one of the underlying human skin (≈1 MPa range). This helps to avoid delamination from the skin due to mechanical mismatch. Moreover, the patch exhibits much higher stretchability: ≈450% compared to ≈30% of the human skin and tensile fatigue testing showed no appreciable signs of mechanical failure of the electrodes after 500 cycles

Thanks to the digital printing, the presented technique can be easily scaled up for rapid fabrication of Taylor-made biostickers patches for different electrophysiological monitoring applications. We showed that the fabricated patches withstand 9 days of continuous use. We did not observe any significant reduction in the signal quality, skin-electrode impedance, or visible deterioration of the biphasic composite after 9 days of continuous wearing, and the electrode skin impedance even decreased in the first 4/5 days of use. During this test, the user performed his normal daily routine, including showering, physical exercise, and other everyday activities

The printed patch attaches directly to a reusable small-sized analog front end which communicates the acquired data in real-time via WiFi. Depending on the patch shape and its positioning in the body, different applications were shown: First, a simple one-lead ECG monitoring setup was presented. The relevant features of the ECG wave could be correctly observed after using the patch for 3 days while doing normal daily routines such as running and taking bath. It was also shown that this system could also monitor the user's respiration pattern, which can be inferred from the ECG amplitude, making this patch a good candidate for sleep apnea monitoring and detection.

This was then extended to a 12-lead ECG, through the EASI electrode montage. Once again, the ECG wave features are observable in the acquired data. Possible use case scenarios include long-term Holter-like heart monitoring with the advantage of the patient being able to shower.

Using a patch that covers the user's forehead and face, we could also record brain activity, eye motion, and muscle activity from chewing. Finally, a patch for recording limb electromyography was fabricated, and the identification of 12 distinct hand gestures was shown. We showed that the fingerprint of the 12 poses are distinct enough from each other to enable good performance of automatic classifiers, and presented improved results compared to the state of the art. For the same gesture, the acquired signals show good repeatability (average similarity coefficient of each pose across three repetitions is >0.7 for all 12 poses for the same subject). These correlation metrics can be further improved by extracting more complex features from the recorded EMG data (for instance, features in the frequency domain) at the cost of increased computation complexity and memory requirements.

A human subject trial was performed on ten volunteers to assess the quality of the conductive polymer-based skin-interfacing electrodes. It was observed that the proposed polymeric electrodes, even with a slightly lower contact area with the skin, show an average impedance in the 1–100 Hz range, which is lower than the Ag/AgCl counterpart. This is attributed to the high conductivity of the composite itself, as well as to the excellent skin-conformability of the fabricated patches, given that the electrodes are not placed in a region with high capillary density. The Ga–In alloy used in the conductive composite was also shown to have a decisive role in improving the quality of the interface by decreasing the electrode-skin impedance when compared with a simple particle-filled Ag–SIS polymer. Furthermore, none of the tested subjects reported any adverse skin reaction or inflammation from contact with the Ag–In–Ga–SIS electrodes. In one case, when the hair density on the test zone was high, the Ag/AgCl electrode performed better than our printed electrodes.

In this study, we have also shown that the bioelectronic patches can be worn for several days without interfering with the quality of signal acquisition and without affecting the user's routine. No deterioration of the conductive polymer was observed, and the electrode skin impedance was even found to decrease after 3 days. In particular, the patch was able to withstand daily showering, running, and other everyday activities, suggesting that these activities are feasible when wearing the adhesive electrode patch and have no noticeable impact on its integrity. Furthermore, none of the tested subjects reported any adverse skin reaction or inflammation from contact with the Ag–In–Ga–SIS electrodes.

Overall, the biostickers presented in this work combine user comfort, durability, strong signal quality, and possibility of direct digital printing for scalable fabrication of taylor-made biostickers. This advancement can pave an important step toward untethering healthcare patients from bulky devices and allowing for domiciliary hospitalization with clinical grade remote patient monitoring.

Further research will focus on integrating adhesive characteristics on the biphasic composites to improve their interfacial properties in subjects with high body hair density and promote an even better conformal contact with the skin's microtexture. Furthermore, to completely avoid the possibility of the thick rigid battery being dethatched from the body due to applied forces from more intense physical exercise, the possibility of integrating a thin printed stretchable battery[4,72] should be investigated. In addition, current and future attempts on direct integration of microchips into stretchable circuits have the potential to contribute toward the next generation of hybrid stretchable circuits that better conform to human skin.[73] Lastly, the development of specific human-machine interface applications employing the proposed patches (facial expression recognition, sleep monitoring, and automatic gesture classification), and further validating data acquisition and usability on a larger population in clinical settings, will be subject of future studies.

4. Experimental Section

Conductive Ink Preparation: The conductive Ag–In–Ga–SIS ink was synthesized as presented in.[32] First SIS (Styrene–Isoprene Copolymer–Aldrich Chemistry) was diluted in Toluene (1:3 wt.%). Silver flakes (Ag071 Technic inc.) were mixed into the SIS solution (2:1 wt.%) using a planetary mixer (Thinky ARE-250) for 3 min at 2000 rpm. Previously

prepared EGaIn (75.5% Ga, 24.5% In) was mixed into the Ag–SIS solution in 2:1 EGaIn:Ag wt.% ratio, and the solution was mixed in the planetary mixer for 3 min at 2000 rpm. The resulting Ag–In–Ga–SIS solution – now with a shiny silvery color – was loaded into a syringe barrel for further printing. For the electrode-skin-impedance tests, a similar formulation of the ink but without the liquid metal was also synthesized for comparison purposes.

E-Patch Fabrication: The Ag–In–Ga–SIS ink was dispensed over a TPU film (Bemis 3412 TPU hotmelt film) following the previously designed paths for the electrodes and interconnects, using a Voltera ink dispensing system (Voltera V-One PCB printer), and the film was let to dry at 60 °C for 10 min (Figure S14A1, Supporting Information). The outline of the patch was then cut using a CO_2 Laser (Universal Laser Systems VLS 3.50), as shown in Figure S14A2 (Supporting Information), leaving the top part of the patch ready (Figure S14A3, Supporting Information). For the bottom part of the patch, a TPU film was adhered on top of a medical-grade skin-compatible adhesive with back paper (3M 1524A Medical Transfer Adhesive) – Figure S14B1 (Supporting Information) – and the outline was cut with the CO2 laser – Figure S14,B2,B3 (Supporting Information). A previously etched interfacing flexible Kapton-copper PCB was then aligned and placed on top of the TPU-adhesive layer, as shown in Figure S14B4 (Supporting Information). The two prepared parts (top and bottom layer) were aligned together with the printed lines facing inward (Figure S14C1, Supporting Information) and heat pressed together (Figure S14C2, Supporting Information) for 30 s at 150 °C using a t-shirt printing press machine (Surpcos HPM-121505). The rigid acquisition PCB was aligned with the flexible PCB in the patch, and both were soldered together, as shown in Figure S14C3 (Supporting Information). Finally, the backing paper of the adhesive was removed (Figure S14C4, Supporting Information), and the system was ready to be laminated to the user's skin.

Biopotential Acquisition, Communication, and Signal Filtering: The rigid circuit board attached to the patch measured 20 × 24 × 10 mm, and weighed only 5.99 g. The PCB was composed of an acquisition layer and a communication layer. The signal acquisition and amplification rely on the ADS1299 module (ADS1299, Texas Instruments), an 8-channel differential amplifier with 24 bit ADC. In this setup, signals were sampled at 250 Hz and amplified 24x, enough for recording even the lowest amplitude surface biopotentials (EEG). The system was powered using a 3.7 V LiPo Battery whose current consumption during normal function was <50 mA. The digitized signals were then passed on to the microcontroller (ESP8266 Expressif Systems), which sent them through the WiFi network (using a UDP protocol) to a receiver (based on the same microcontroller). The receiver dongle sent the incoming values from the WiFi network to the serial port for visualization, recording, and further processing, as shown in Figure S15 (Supporting Information). The incoming signals from the serial port were saved and later filtered in MATLAB using a notch filter (60 Hz) and High/Low pass second-order Butterworth filters as needed for each monitored signal. For ECG, the relevant frequencies were assumed to be in the 5–55 Hz band. For EEG, EOG, and EMG, the relevant frequencies were considered to be in the 2–100 Hz band. The 12-lead ECG signals ($\boldsymbol{v}$) can be derived from the acquired EASI potentials ($\boldsymbol{v}_{\mathbf{ES}}$, $\boldsymbol{v}_{\mathbf{AS}}$, $\boldsymbol{v}_{\mathbf{AI}}$) through the following equation:

$$v = a.v_{ES} + b.v_{AS} + c.v_{AI} \tag{2}$$

The fixed coefficients ($\boldsymbol{a}$, $\boldsymbol{b}$, $\boldsymbol{c}$) for the calculation of each lead are shown in **Table 1**.

Electrode-Skin Impedance Measurement: Patches with three Ag–In–Ga–SIS electrodes were fabricated (Figure S16, Supporting Information), as well as patches with Ag–SIS (without the liquid metal). The impedance on these, as well as Ag/AgCl electrodes (3 M Red Dot) was measured, using a PalmSens4 impedance analyzer. 50 impedance points (≈9.8 per decade) were measured between 10^0 and 10^5 Hz for each bode plot.

Before placing each set of electrodes on the right inner forearm of the volunteer, the skin was cleaned by wiping with rubbing alcohol and driedfor 1 min. The electrode set to be recorded was then placed and left to rest for 1 min, and the impedance measurement was taken.

Table 1. Transformation coefficients for approximation of the 12-lead ECG through acquired EASI signals.

Lead (v)	a	b	c
I	0.026	−0.174	0.701
II	−0.002	1.098	−0.763
III	−0.028	1.272	−1.464
aVR	−0.012	−0.462	0.031
aVL	0.027	−0.723	1.082
aVF	−0.015	1.185	1.114
V1	0.641	−0.391	0.080
V2	1.229	−1.050	1.021
V3	0.947	−0.539	0.987
V4	0.525	0.004	0.841
V5	0.179	0.278	0.630
V6	−0.043	0.431	0.213

After the measurement was complete, the electrodes were removed, and any residue of adhesive was wiped off with rubbing alcohol. The process was then repeated for other electrodes. The equivalent circuit components for the electrode–skin interface were approximated by fitting the obtained bode plots to the equivalent impedance expression through the Levenberg–Marquardt algorithm (damped least-squares), integrated into the PalmSens PSTrace software.

Ten volunteers participated in this study, which was approved by the Carnegie Mellon University Institutional Review Board (STUDY2022_00000015) in accordance with the US HHS regulations for the protection of human subjects in research at 45CFR 46. Informed consent was obtained from all the participants, and all experiments were performed in accordance with the applicable regulations.

SNR Calculations: After filtering the acquired ECG signals, signal-to-noise ratio calculations were performed in Matlab. The function used for the calculation, *snr(s,n)*, was based on the formula from Equation 3:

$$20log_{10}\left(\frac{rssq(s)}{rssq(n)}\right) \tag{3}$$

where *rssq*(*s*) corresponds to the root-sum-of-squares of the clean signal amplitude and *rssq*(*n*) corresponds to the root-sum-of-squares of the removed noise amplitude.

Tensile Testing: To characterize the mechanical performance of the materials, a "dog bone" shape was used following the CASTM D 412 standard (dimensions shown in Figure S3, Supporting Information). For tensile testing, an Instron5969 with a 10 N load cell was used.

For the quasi-static break test a strain rate of ≈0.002 s^{-1} was used, while for the cyclic loading tests, 500 cycles of 30% strain were performed at a rate of ≈0.094 cycles s^{-1}.

Statistical Analysis: Unless otherwise stated, one measurement per subject/sample was taken in each subject. Data treatment, analysis, and plotting of all data were performed in Matlab_R2020b.

Supporting Information

Supporting Information is available from the Wiley Online Library or from the author.

Acknowledgements

Support for this research was provided by the Fundação para a Ciência e a Tecnologia (Portuguese Foundation for Science and

Technology) through the Carnegie Mellon Portugal Program under Grant SFRH/BD/150691/2020. Funding also came from the CMU-Portugal project WoW (45913), which had the support of the European Regional Development Fund (ERDF) and the Portuguese State through Portugal 2020 and COMPETE 2020, as well as the Nano-Bio Materials Consortium (NBMC), sponsored by the US Air Force Research Laboratory (AFRL) in partnership with SEMI.

Conflict of Interest

The authors declare no conflict of interest.

Data Availability Statement

The data that support the findings of this study are available from the corresponding author upon reasonable request.

Keywords

bioelectronics, biomonitoring, e-health, electrophysiology, epidermal electronics, IoMT, stretchable circuits, wearables

Received: May 25, 2022
Revised: July 18, 2022
Published online:

[1] S. M. A. Iqbal, I. Mahgoub, E. Du, M. A. Leavitt, W. Asghar, *npj Flexible Electron.* **2021**, *5*, 9.
[2] M. A. Yokus, J. S. Jur, *IEEE Trans. Biomed. Eng.* **2016**, *63*, 423.
[3] J. Alberto, C. Leal, C. Fernandes, P. A. Lopes, H. Paisana, A. T. d. Almeida, M. Tavakoli, *Sci. Rep.* **2020**, *10*, 5539.
[4] C. Leal, P. A. Lopes, A. Serra, J. F. J. Coelho, A. T. d. Almeida, M. Tavakoli, *ACS Appl. Mater. Interfaces* **2020**, *12*, 3407.
[5] H. Wang, J. Wang, D. Chen, S. Ge, Y. Liu, Z. Wang, X. Zhang, Q. Guo, J. Yang, *IEEE Sens. J.* **2022**, *22*, 3817.
[6] D. G. Marques, P. A. Lopes, A. T. d. Almeida, C. Majidi, M. Tavakoli, *Lab Chip* **2019**, *19*, 897.
[7] M. Tavakoli, C. Benussi, J. L. Lourenco, *Expert Syst. Appl.* **2017**, *79*, 322.
[8] S. Maragliulo, P. F. A. Lopes, L. B. Osorio, A. T. D. Almeida, M. Tavakoli, *IEEE Sens. J.* **2019**, *1*, 10187.
[9] G. M. Paul, F. Cao, R. Torah, K. Yang, S. Beeby, J. Tudor, *IEEE Sensors* **2014**, *14*, 393.
[10] S. Myllymaa, P. Lepola, J. Toyras, T. Hukkanen, E. Mervaala, R. Lappalainen, K. Myllymaa, *J. Neurosci. Methods* **2013**, *215*, 103.
[11] D. Looney, P. Kidmose, C. Park, M. Ungstrup, M. Rank, K. Rosenkranz, D. Mandic, *IEEE Pulse* **2012**, *3*, 32.
[12] M. R. Carneiro, A. T. d. Almeida, M. Tavakoli, *IEEE Sens. J.* **2020**, *1*, 15107.
[13] P. Lepola, S. Myllymaa, J. Toyras, A. Muraja-Murro, E. Mervaala, R. Lappalainen, K. Myllymaa, *Sens. Actuators, A* **2014**, *213*, 19.
[14] S. L. Kappel, M. L. Rank, H. O. Toft, M. Andersen, P. Kidmose, *IEEE Trans. Biomed. Eng.* **2019**, *66*, 150.
[15] S. K. Ameri, M. Kim, I. A. Kuang, W. K. Perera, M. Alshiekh, H. Jeong, U. Topcu, D. Akinwande, N. Lu, *npj 2D Mater. Appl.* **2018**, *2*, 19.
[16] M. R. Carneiro, M. Tavakoli, *IEEE Sens. J.* **2021**, *21*.
[17] Z. Sang, K. Ke, I. Manasâ Zloczower, *Small* **2019**, *15*, 1903487.
[18] D. Patron, W. Mongan, T. P. Kurzweg, A. Fontecchio, G. Dion, E. K. Anday, K. R. Dandekar, *IEEE Trans. Biomed. Circuits Syst.* **2016**, *10*, 1047.
[19] S. Yao, P. Swetha, Y. Zhu, *Adv. Healthcare Mater.* **2018**, *7*, 1700889.
[20] W. Gao, H. Ota, D. Kiriya, K. Takei, A. Javey, *Acc. Chem. Res.* **2019**, *52*, 523.
[21] S. K. Ameri, R. Ho, H. Jang, L. Tao, Y. Wang, L. Wang, D. M. Schnyer, D. Akinwande, N. Lu, *ACS Nano* **2017**, *11*, 7634.
[22] G. Wang, S. Zhang, S. Dong, D. Lou, L. Ma, X. Pei, H. Xu, U. Farooq, W. Guo, J. Luo, *IEEE Trans. Biomed. Eng.* **2019**, *66*, 1000.
[23] L. Santos, N. Carbonaro, A. Tognetti, J. L. González, E. D. l. Fuente, J. Fraile, J. Pérez-Turiel, *Technologies* **2018**, *6*, 8.
[24] Y. Jiao, C. W. Young, S. Yang, S. Oren, H. Ceylan, S. Kim, K. Gopalakrishnan, P. C. Taylor, L. Dong, *IEEE Sens. J.* **2016**, *16*, 7870.
[25] A. F. Silva, M. Tavakoli, *Sensors* **2020**, *20*, 6835.
[26] M. A. Buhagiar, J. M. Naylor, I. A. Harris, W. Xuan, F. Kohler, R. Wright, R. Fortunato, *JAMA, J. Am. Med. Assoc.* **2017**, *317*, 1037.
[27] D. M. Levine, K. Ouchi, B. Blanchfield, A. Saenz, K. Burke, M. Paz, K. Diamond, C. T. Pu, J. L. Schnipper, *Ann. Intern. Med.* **2020**, *172*, 77.
[28] S. Hong, S. Lee, D.-H. Kim, *Proc. IEEE* **2019**, *107*, 2185.
[29] Y. Zhao, A. Kim, G. Wan, B. C. K. Tee, *Nano Convergence* **2019**, *6*, 25.
[30] D.-H. Kim, N. Lu, R. Ma, Y.-S. Kim, R.-H. Kim, S. Wang, J. Wu, S. M. Won, H. Tao, A. Islam, K. J. Yu, T. Kim, R. Chowdhury, M. Ying, L. Xu, M. Li, H.-J. Chung, H. Keum, M. McCormick, J. A. Rogers, *Epidermal Electronics. Science* **2011**, *333*, 838.
[31] M. Tavakoli, M. H. Malakooti, H. Paisana, Y. Ohm, D. G. Marques, P. A. Lopes, A. P. Piedade, A. T. Almeida, C. Majidi, *Adv. Mater.* **2018**, *30*, 1801852.
[32] P. A. Lopes, D. F. Fernandes, A. F. Silva, D. G. Marques, A. T. d. Almeida, C. Majidi, M. Tavakoli, *ACS Appl. Mater. Interfaces* **2021**, *13*, 14552.
[33] W. Wu, *Sci. Technol. Adv. Mater.* **2019**, *20*, 187.
[34] R. K. Kramer, C. Majidi, R. J. Wood, *Adv. Funct. Mater.* **2013**, *23*, 5292.
[35] Y. Zhao, Y. J. Tan, W. Yang, S. Ling, Z. Yang, J. T. Teo, H. H. See, D. K. H. Lee, D. Lu, S. Li, X. Zeng, Z. Liu, B. C. K. Tee, *Adv. Healthcare Mater.* **2021**, *10*, 2100221.
[36] W. Zu, Y. Ohm, M. R. Carneiro, M. Vinciguerra, M. Tavakoli, C. Majidi, *Adv. Mater. Technol.* **2022**, https://doi.org/10.1002/admt.202200534.
[37] N. Kazem, T. Hellebrekers, C. Majidi, *Adv. Mater.* **2017**, *29*, 1605985.
[38] S. Liu, D. S. Shah, R. Kramer-Bottiglio, *Nat. Mater.* **2021**, *20*, 851.
[39] M. Baharfar, K. Kalantar-Zadeh, *ACS Sens.* **2022**, *7*, 386.
[40] A. d. Santos, N. Pinela, P. Alves, R. Santos, E. Fortunato, R. Martins, H. Águas, R. Igreja, *Proceedings* **2018**, *2*, 1039.
[41] R. P. Rocha, P. A. Lopes, A. T. De Almeida, M. Tavakoli, C. Majidi, *J. Micromech. Microeng.* **2018**, *28*, 034001.
[42] G. I. Hay, P. S. A. Evans, D. J. Harrison, D. Southee, G. Simpson, P. M. Harrey, *IEEE Sens. J.* **2005**, *5*, 864.
[43] I. D. Joshipura, H. R. Ayers, C. Majidi, M. D. Dickey, *J. Mater. Chem. C* **2015**, *3*, 3834.
[44] J. Wissman, T. Lu, C. Majidi, in *Proceedings of IEEE Sensors*, IEEE Computer Society, Washington, DC **2013**.
[45] T. Lu, L. Finkenauer, J. Wissman, C. Majidi, *Adv. Funct. Mater.* **2014**, *24*, 3351.
[46] D. F. Fernandes, C. Majidi, M. Tavakoli, *J. Mater. Chem. C* **2019**, *7*, 14035.
[47] H. Tian, Y. Shu, X.-F. Wang, M. A. Mohammad, C. Li, Y. Yang, T.-L. Ren, *Tech. Dig. – Int. Electron Devices Meet. IEDM*, **2015**, p. 15.1.1.
[48] M. R. Carneiro, C. Majidi, M. Tavakoli, *Adv. Eng. Mater.* **2021**, *24*, 2100953.
[49] P. A. Lopes, B C. Santos, A T. De Almeida, M. Tavakoli, *Nat. Commun.* **2021**, *12*, 4666.
[50] D. F. Fernandes, C. Majidi, M. Tavakoli, *J. Mater. Chem. C* **2019**, *7*, 14035.
[51] F. M. Carvalho, P. Lopes, M. Carneiro, A. N. Serra, J. Coelho, A. T. d. Almeida, M. Tavakoli, *ACS Appl. Electron. Mater.* **2020**, *2*, 3390.

[52] Y. Ohm, C. Pan, M. J. Ford, X. Huang, J. Liao, C. Majidi, *Nat. Electron.* **2021**, *4*, 185.
[53] L. Bareket, L. Inzelberg, D. Rand, M. David-Pur, D. Rabinovich, B. Brandes, Y. Hanein, *Sci. Rep.* **2016**, *6*, 25727.
[54] P. A. Lopes, H. Paisana, A. T. D. Almeida, C. Majidi, M. Tavakoli, **2018**, *10*, 38760
[55] L. Zhang, K. S. Kumar, H. He, C. J. Cai, X. He, H. Gao, S. Yue, C. Li, R. C.-S. Seet, H. Ren, J. Ouyang, *Nat. Commun.* **2020**, *11*, https://doi.org/10.1038/s41467-020-18503-8.
[56] P. A. Lopes, D. V. Gomes, D. G. Marques, P. Faia, J. Gois, T. F. Patricio, J. Coelho, A. Serra, A. T. d. Almeida, C. Majidi, M. Tavakoli, *Adv. Healthcare Mater.* **2019**, *8*, 1900234.
[57] L. M. Ferrari, S. Sudha, S. Tarantino, R. Esposti, F. Bolzoni, P. Cavallari, C. Cipriani, V. Mattoli, F. Greco, *Adv. Sci.* **2018**, *5*, 1700771.
[58] Y. Mengüç, Y.-L. Park, H. Pei, D. Vogt, P. M. Aubin, E. Winchell, L. Fluke, L. Stirling, R. J. Wood, C. J. Walsh, *Int. J. Rob. Res.* **2014**, *33*, 1748.
[59] S. Wagner, S. Bauer, *MRS Bull.* **2012**, *37*, 207.
[60] M. D. Dickey, *Adv. Mater.* **2017**, *29*, 1606425.
[61] D. Rus, M. T. Tolley, *Nature* **2015**, *521*, 467.
[62] A. Albulbul, *Bioengineering* **2016**, *3*, 20.
[63] R. S. Timsit, *IEEE Trans. Compon. Packag. Technol.* **1999**, *22*, 85.
[64] K. Doudrick, S. Liu, E. M. Mutunga, K. L. Klein, V. Damle, K. K. Varanasi, K. Rykaczewski, *Langmuir* **2014**, *30*, 6867.
[65] F. G. Yanowitz, *Introduction to ECG Interpretation*, Intermountain Healthcare, Salt Lake City, USA **2018**.
[66] J. Ng, J. J. Goldberg, *The Phyisiological Measurement Handbook – Cardiology*, CRC Press, Boca Raton, USA **2014**.
[67] D. Jenkins, S. Gerred, *ECG Library*, https://ecglibrary.com/norm.php
[68] K. Kirschfeld, *Biol. Cybern.* **2005**, *92*, 177.
[69] S. Orguc, H. S. Khurana, K. M. Stankovic, H. S. Leel, A. P. Chandrakasan, in *Annu. Int. Conf. IEEE Eng. Med. Biol. – Proc*, EMBS, Baltimore, USA **2018**.
[70] M. F. Rabbi, C. Pizzolato, D. G. Lloyd, C. P. Carty, D. Devaprakash, L. E. Diamond, *Sci. Rep.* **2020**, *10*, 8266.
[71] G. Rosati, G. Cisotto, D. Sili, L. Compagnucci, C. De Giorgi, E. F. Pavone, A. Paccagnella, V. Betti, *Sci. Rep.* **2021**, *11*, https://doi.org/10.1038/s41598-021-94526-5.
[72] G. Costa, P. A. Lopes, A. L. Sanati, A. F. Silva, M. C. Freitas, A. T. d. Almeida, M. Tavakoli, *Adv. Funct. Mater.* **2022**, *32*, 2113232.
[73] M. Tavakoli, P. Alhais Lopes, A. Hajalilou, A. F. Silva, M. R. Carneiro, J. Carvalheiro, J. M. Pereira, A. T. d. Almeida, *Adv. Mater.* **2022**, *34*, 2203266.